

Dual-Satellite Geolocation of Terrestrial GNSS Jammers from Low Earth Orbit

Zachary Clements, Todd E. Humphreys
Radionavigation Laboratory
The University of Texas at Austin
Austin, TX, USA
zclements@utexas.edu
todd.humphreys@utexas.edu

Patrick Ellis
Advanced Signal Processing Group
Spire Global
Vienna, VA, USA
patrick.ellis@spire.com

Abstract—This paper explores two-step and direct geolocation of terrestrial Global Navigation Satellite System (GNSS) jammers from Low Earth Orbit (LEO). Within the past decade, there has been a sharp increase in GNSS outages due to deliberate GNSS jamming. Receivers in LEO are uniquely situated to detect, classify, and geolocate terrestrial GNSS jammers. The conventional two-step geolocation method first estimates the differential delay and differential Doppler, then uses a time history of these to estimate the transmitter location. By contrast, direct geolocation is a single-step search over a geographical grid that enables estimation of the transmitter location directly from the observed signals. Signals from narrowband, matched-code, and chirp jammers recently captured in the GNSS frequency bands by two time-synchronized LEO receivers over the Eastern Mediterranean are analyzed and the emitters geolocated. It is demonstrated that the direct approach is effective even for low signal-to-noise ratio interference signals based on short captures with multiple emitters. Moreover, the direct approach enables geolocation of multiple emitters with cyclostationary signals (e.g., chirp jammers), whereas the two-step method struggles in such cases to associate emitters with their corresponding structures in differential delay and Doppler space.

Index Terms—emitter geolocation; interference localization; spectrum monitoring.

I. INTRODUCTION

Global Navigation Satellite Systems (GNSS) such as GPS provide meter-accurate positioning while offering global accessibility and all-weather, radio-silent operation. However, GNSS is fragile: its service is easily denied by jammers or deceived by spoofers [1]–[3]. GNSS signals are especially vulnerable to jamming because they are extremely weak: near the surface of Earth, they have no more flux density than light received from a 50 W bulb at a distance of 2000 km [4]. Furthermore, GNSS jammers are easily accessible and low cost, threatening GNSS-reliant systems [5], [6]. Without proper countermeasures, victim GNSS receivers can be rendered useless.

The civilian maritime and airline industries frequently encounter GNSS jamming and spoofing. Corrupted Automatic Identification System (AIS) and Automatic Dependent Surveillance-Broadcast (ADS-B) messages from surface vessels and aircraft are often reported. Irregularities in AIS and ADS-B reports are often indicative of GNSS interference.

Geolocation of GNSS jammers with ADS-B data is possible, but only coarse jammer position estimates are achievable [7], [8].

Recently, the German Aerospace Center (DLR) performed a data collection flight over the Eastern Mediterranean to study the behavior of regular avionics and aviation-grade GNSS receivers under jamming conditions [9]. The DLR also conducted an international maritime measurement campaign to detect GNSS interference [10]. In both studies, the recorded data showed evidence of high-power GNSS jammers, including a chirp jammer centered at the GPS L1 frequency in the Eastern Mediterranean.

GNSS jamming waveforms can take several forms, including tones, chirps, pulses, and matched-code interference [11]. A first step to developing situational awareness and eliminating GNSS interference is geolocating the emitters involved. It was shown that a network of ground-based receivers could track and geolocate chirp-style jamming signals in [12], and matched-code jamming signals in [13]. The more general case of localizing an emitter transmitting an arbitrary wideband signal with terrestrial and airborne receivers has been extensively studied [14]–[17]. However, because the receivers were either at fixed locations or tactically deployed in the nearby airspace, only emitters in the immediate area could be geolocated. There remains a need for global, persistent, low-latency, and accurate GNSS interference detection and localization.

Receivers based in Low Earth Orbit (LEO) are a proven asset for detecting, classifying, and geolocating terrestrial GNSS interference [18]–[20]. Emitter geolocation from LEO offers worldwide coverage with a frequent refresh rate, making it possible to maintain a common operating picture of terrestrial sources of interference, e.g., GNSS jammers and spoofers. Moreover, LEO satellites' stand-off distance from terrestrial interference sources typically permits tracking authentic GNSS signals, enabling precise time-tagged data captures from time-synchronized LEO-based receivers and precise orbit determination. LEO constellations with distributed time-synchronized receivers can provide unprecedented emitter geolocation. Unsurprisingly, several commercial enterprises have seized the opportunity to provide spectrum monitoring and emitter geolocation as a service (e.g., Spire Global and Hawkeye360).

Accurate single-satellite-based emitter geolocation is possible from Doppler measurements alone, provided the emitter’s carrier can be extracted [19]–[21]. Performance bounds and error characterization for Doppler-based single-satellite geolocation are presented in [22] [23]. However, accurately locating emitters with arbitrary waveforms using a single LEO receiver is impossible in general: if the signal’s carrier cannot be tracked, only coarse received-signal-strength techniques can be applied for geolocation.

On the other hand, geolocation of emitters producing arbitrary wideband signals is possible and has been extensively studied [14], [24], [25]. Multiple time-synchronized receivers can exploit time- and frequency-difference of arrival (T/FDOA) measurements to estimate the emitter location. Geolocation based on T/FDOA is typically a two-step process. First, a time series of T/FDOA measurements is produced by correlating captured signals against another. Second, the time series is fed to a nonlinear estimation algorithm to geolocate the source. Two-step T/FDOA has been previously applied for terrestrial emitter localization from geostationary orbit [26].

One weakness of two-step geolocation is that it ignores the constraint that all measurements must be consistent with a single position in the case of a stationary emitter, or a single trajectory in the case of a moving emitter [27]. This means that the T/FDOA measurements obtained in the first step are not guaranteed to intersect at a single location or along a single trajectory. A second weakness of the two-step approach is that interference signals exhibiting cyclostationarity—such as chirp jammers—give rise to structures in the T/FDOA measurement domain that make it harder to track individual emitters. Identification and tracking becomes especially challenging when there are multiple cyclostationary emitters with overlapping frequency content and a wide range of received power, in which case the T/FDOA measurement domain becomes highly structured with features ambiguously related to the emitters involved.

Another multi-receiver technique is direct geolocation, which is a single-step search over a geographical grid to estimate a transmitter’s location directly from the observed signals [27]–[31]. In direct geolocation, the TDOA and FDOA are directly parameterized for a single geographical point, given knowledge of the receivers’ position, velocity, and clock states. Direct geolocation outperforms the two-step method in low signal-to-noise ratio (SNR) environments and in short-data-capture scenarios, making it ideal for LEO-based geolocation. Furthermore, as will be shown in this paper, direct geolocation is better suited for processing captures with cyclostationary signals from multiple emitters, because rather than searching in the T/FDOA measurement domain cluttered by overlapping structures, it searches in the position domain, where individual emitters are separated by their physical distance, irrespective of any time correlation in their signals.

This paper makes three primary contributions. First, it develops and presents algorithms—from raw samples to final emitter position estimate—for two-step and direct geolocation. Prior literature did not consider time-varying FDOA, whereas

this paper does. Secondly, it investigates how the time-domain properties of the transmitted signal manifest in the complex ambiguity function (CAF) of the two-step approach. Prior research did not take into account arbitrary time-correlated signals. Finally, this paper demonstrates two-step and direct geolocation on raw intermediate frequency (IF) samples recorded from Spire Global’s LEO constellation. For the first time in the open literature, real-world GNSS narrowband, matched-code, and chirp jamming signals captured by two time-synchronized LEO receivers are characterized and their emitters geolocated.

II. MEASUREMENT MODEL

Consider the following model for a signal transmitted by a terrestrial stationary emitter where $s(t)$ is the complex envelope, f_c is the center frequency, and the bandwidth of $s(t)$ is $B \ll f_c$:

$$x(t) = s(t)e^{j2\pi f_c t} \quad (1)$$

This analytic signal model is valid when the complex envelope varies slowly with respect to the center frequency, which applies to the GPS L1 (1575.42 MHz) and L2 (1227.6 MHz) frequencies.

When a moving receiver receives this signal, there is a time delay τ due to the propagation time, as well as a Doppler shift f_d due to the relative motion between emitter and receiver. Doppler effects arising from relative motion between a LEO receiver and a ground transmitter are considerable in the L-band for the Earth-to-LEO channel. Thus, a comprehensive Doppler model is required, consisting of both a frequency shift and compression/dilation of the baseband signal. Over short intervals, the line of sight velocity v_{LOS} can be modeled as constant (the full time-varying nature of v_{LOS} will be explored in a later section). Additionally the transmitter and receiver clock offset rate gives rise to an effect identical to motion-induced Doppler. Let c represent the speed of light. The term $\beta \triangleq v_{\text{LOS}}/c$ is introduced to parameterize the additive effects of relative motion and clock-error-induced Doppler. β and f_d are related by $f_d = -f_c\beta$. The received complex signal at the i th receiver after downconversion by a known carrier frequency f_c at time t can be modeled as

$$y_i(t) = s((t - \tau_i)(1 - \beta))e^{j2\pi f_{d,i}t} \quad (2)$$

A. TDOA and FDOA Measurement Model

Let $\mathbf{p}_i(t)$ and $\mathbf{v}_i(t)$ denote the position and velocity vector for the i th receiver, and \mathbf{p}_e denote the emitter’s position vector, all in a common rectangular coordinate frame. In this model, the emitter is assumed to be stationary. Ionospheric and tropospheric delay are ignored because they will be substantially canceled in the differencing to follow. The time of arrival (TOA) at the i th receiver of the signal transmitted from the emitter at time t is modeled as

$$\begin{aligned} \tau_i(t) &= \frac{1}{c} \sqrt{(\mathbf{p}_i(t) - \mathbf{p}_e(t - \tau))^\top (\mathbf{p}_i(t) - \mathbf{p}_e(t - \tau))} \\ &= \frac{1}{c} \sqrt{\mathbf{r}_i^\top(t) \mathbf{r}_i(t)} \end{aligned} \quad (3)$$

where the range vector $\mathbf{r}_i(t)$ between the emitter and the i th receiver is

$$\mathbf{r}_i(t) = \mathbf{p}_i(t) - \mathbf{p}_e(t - \tau) \quad (4)$$

The range between the emitter and the i th receiver is related to τ_i and \mathbf{r}_i by

$$\rho_i(t) = c\tau_i(t) = \sqrt{\mathbf{r}_i^T(t)\mathbf{r}_i(t)} \quad (5)$$

Finally, the unit vector from emitter position to the i th receiver position is defined as

$$\hat{\mathbf{r}}_i = \mathbf{r}_i(t)/\rho_i(t) \quad (6)$$

Different LEO-based receivers will receive the same signal at different times due to the differing geometry between receivers. Assuming the receivers are synchronized to GPS time, the time difference of arrival (TDOA) of the same signal between the i th and j th receiver is defined as

$$\Delta\tau(t) = \tau_2(t) - \tau_1(t) \quad (7)$$

which can be converted to a range difference by multiplying by the speed of light.

The frequency of arrival (FOA) measurement is synonymous with the received Doppler of a signal. For a stationary emitter, the FOA on the i th moving receiver is composed of three components: (1) the range-rate between the emitter and receiver $\hat{\mathbf{r}}_i^T(t)\mathbf{v}_i(t)$, (2) the clock offset rate of the receiver $\delta\dot{t}_i(t)$, and (3) the clock offset rate of the emitter $\delta\dot{t}_e(t)$. The FOA at the i th receiver is modeled as

$$f_{d,i}(t) = -\frac{1}{\lambda}\hat{\mathbf{r}}_i^T(t)\mathbf{v}_i(t) - \frac{c}{\lambda}\{\delta\dot{t}_i(t) - \delta\dot{t}_e(t)[1 - \delta\dot{t}_i(t)]\} \quad (8)$$

Different LEO receivers will also receive the same signal at different frequencies due to the differing instantaneous range-rates and receiver clock offset rates. Let $\Delta\tilde{f}(t)$ denote the frequency difference of arrival that includes the receivers' clock offset rates.

$$\begin{aligned} \Delta\tilde{f}(t) &= f_{d,2}(t) - f_{d,1}(t) \\ &\approx -\frac{1}{\lambda}\{\hat{\mathbf{r}}_2^T(t)\mathbf{v}_2(t) - \hat{\mathbf{r}}_1^T(t)\mathbf{v}_1(t)\} - \frac{c}{\lambda}\{\delta\dot{t}_2(t) - \delta\dot{t}_1(t)\} \end{aligned} \quad (9)$$

An advantageous feature of $\Delta\tilde{f}(t)$ is that the clock offset rate from the emitter is removed: because the same emitter clock offset rate is observed at each receiver, it gets canceled out in the differencing. The approximation disregards the $\delta\dot{t}_e(t)$ and $\delta\dot{t}_i(t)$ cross terms, as they are negligible. The frequency difference of arrival (FDOA) $\Delta f(t)$ with compensated receiver clock offset rate between the first and second receiver is defined as

$$\begin{aligned} \Delta f(t) &= \Delta\tilde{f}(t) + \underbrace{\frac{c}{\lambda}\{\delta\dot{t}_2(t) - \delta\dot{t}_1(t)\}}_{\text{known}} \\ &= -\frac{1}{\lambda}\{\hat{\mathbf{r}}_2^T(t)\mathbf{v}_2(t) - \hat{\mathbf{r}}_1^T(t)\mathbf{v}_1(t)\} \end{aligned} \quad (10)$$

The onboard GNSS navigation solution of each receiver outputs an estimate of the receiver clock offset rate $\delta\dot{t}$ at each GNSS measurement epoch. This means that the clock offset rate at each receiver is known and can be compensated for, making the FDOA measurement the difference between range-rates scaled by the negative reciprocal of wavelength.

B. The Generalized Cross-Correlation Function

Assume that all receivers are synchronized to GPS time and clock errors have been compensated for. The generalized cross-correlation function (GCCF) for a pair of received complex baseband signals $y_1(t)$ and $y_2(t)$ is

$$S(y_1(t), y_2(t), \tau_1(t), \tau_2(t)) \triangleq \int_0^T y_1(t - \tau_1(t))y_2^*(t - \tau_2(t))e^{j2\pi f_c[\tau_1(t) - \tau_2(t)]} dt \quad (11)$$

where T is the integration interval. The more familiar complex ambiguity function (CAF) from the radar literature [32] with constant delay τ_0 and Doppler f_d is

$$\tilde{S}(y_1(t), y_2(t), \tau_0, f_d) \triangleq \int_0^T y_1(t)y_2^*(t + \tau_0)e^{-j2\pi f_d t} dt \quad (12)$$

This can be expressed in terms of the GCCF by $\tau_1(t) = 0$ and $\tau_2(t) = \tau_0 + \frac{f_d}{f_c}t$. Over short intervals, the errors introduced by assuming the delay τ_0 and Doppler f_d to be constant are negligible [28]. The maximum coherent integration length T is typically dictated by the receivers' dynamics and clock variations. If the receivers are assumed to be LEO-based and equipped with a temperature-compensated crystal oscillator (TCXO) clock, T should be no more than 40 ms. The discrete-time CAF can be efficiently evaluated with the Fast Fourier Transform (FFT) and the presence of emitters can be visualized in the delay-Doppler domain.

Consider a pair of spatially separated receivers with received signals $y_1(t)$ and $y_2(t)$. If there is only a single emitter, it is shown in [28], [33] that the delay and Doppler that maximizes the magnitude of the CAF, denoted as $\tau_0 = \Delta t$ and $f_d = \Delta f$, are the corresponding maximum likelihood estimates (MLE) of the time and frequency difference of arrival between a pair of receivers. Fig. 1 is an example CAF.

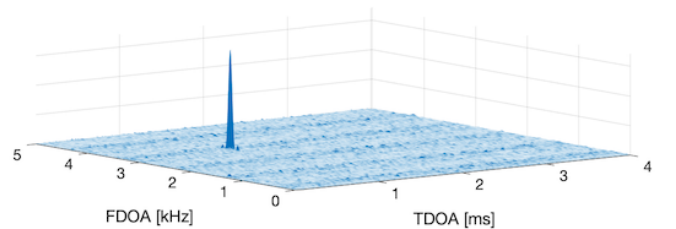


Fig. 1: Example CAF for a single wideband emitter without any cyclostationary properties. The maximum value corresponds to the MLE of TDOA and FDOA.

Several complications arise when there are multiple emitters present. In this case, the auto-ambiguity terms generated

by each emitter's waveform may interfere with each other, leading to biases in the T/FDOA estimate [28]. Moreover, the height of an emitter's peak in the CAF is determined by the emitter's transmit power. Weaker emitters will have smaller peaks, leading to possible missed detections in the presence of stronger emitters. Furthermore, transmitted signals exhibiting cyclostationarity give rise to additional structures in the CAF, making individual peaks more difficult to track.

III. EMITTER GEOLOCATION WITH TWO-STEP AND ONE-STEP TECHNIQUES

A. Two-step Geolocation

In the traditional two-step geolocation approach, a time series of T/FDOA measurements is first obtained by repeated CAF generation and peak tracking. The CAF is computed at each time instant a T/FDOA measurement is desired. For a single emitter, the TDOA and FDOA pair corresponding to the peak in the CAF are the T/FDOA measurements at that measurement epoch. For model simplicity, TDOAs can be converted to range difference in meters by scaling them by the speed of light. FDOAs can be converted to range-rate in meters per second by scaling by $-\lambda$. In this section, TDOAs and FDOAs are assumed to be converted into m and m/s respectively, between two receivers.

All dual-satellite emitter geolocation techniques assume the emitter altitude is constrained to strengthen observability. One way to implement the altitude constraint is incorporating it as a pseudo-measurement as in [19]. This paper takes a more straightforward approach: the receivers' positions and velocity are converted into the East-North-Up (ENU) frame centered at the current best estimate of the emitter's position, i.e., $\mathbf{p}_e = [0, 0, 0]^T$. The emitter's position is now in a state that is easily related to the measurement model and the altitude is constrained because the vertical coordinate is held to 0.

A nonlinear least-squares (NLLS) estimator is used to solve for the position of the transmitter. The standard weighted nonlinear least-squares cost function is

$$J(\mathbf{x}) = \frac{1}{2} [\mathbf{z} - \mathbf{h}(\mathbf{x})]^T R^{-1} [\mathbf{z} - \mathbf{h}(\mathbf{x})] \quad (13)$$

where \mathbf{x} is the 2×1 state representing the emitter's position, and x and y respectively denote the displacement east and west from the current best estimate

$$\mathbf{x} = \begin{bmatrix} x \\ y \end{bmatrix} \quad (14)$$

\mathbf{z} is the $2N \times 1$ T/FDOA measurement vector

$$\mathbf{z} = \begin{bmatrix} c\Delta\tau_1 \\ \vdots \\ c\Delta\tau_N \\ -\lambda\Delta f_1 \\ \vdots \\ -\lambda\Delta f_N \end{bmatrix} \quad (15)$$

$\mathbf{h}(\mathbf{x})$ is the $2N \times 1$ nonlinear measurement model function

$$\mathbf{h}(\mathbf{x}) = \begin{bmatrix} c\Delta\bar{\tau}_1 \\ \vdots \\ c\Delta\bar{\tau}_N \\ -\lambda\Delta\bar{f}_1 \\ \vdots \\ -\lambda\Delta\bar{f}_N \end{bmatrix} \quad (16)$$

where $\Delta\bar{\tau}_k$ and $\Delta\bar{f}_k$ are the estimates of $\Delta\tau_k$ and Δf_k at the current best estimate of the state, and k denotes the k th T/FDOA measurement pair. R is the $2N \times 2N$ measurement covariance matrix with the variance of the TDOA measurements $\sigma_{\Delta\tau}^2$ along the first N diagonal elements and the variance of the FDOA measurements $\sigma_{\Delta f}^2$ along the second N diagonal elements.

The 1×2 Jacobian for the k th TDOA measurement is

$$c \frac{d\Delta\tau_k}{d\mathbf{x}} = -[\hat{\mathbf{r}}_2 - \hat{\mathbf{r}}_1]^T \Xi \quad (17)$$

where

$$\Xi = \begin{bmatrix} 1 & 0 \\ 0 & 1 \\ 0 & 0 \end{bmatrix} \quad (18)$$

The matrix Ξ is used to extract the first two elements because they correspond to the partials with respect to the unknown elements of the emitter position vector \mathbf{x} .

The Jacobian for the k th FDOA measurement is a little more involved and the full derivation of the derivative of the Doppler measurement can be found in [34]. It can be shown that the 1×3 Jacobian of a range-rate measurement between the i th receiver and the emitter, with respect to the three dimensional position vector at the k th measurement is

$$\frac{d\hat{\rho}_i}{d\mathbf{r}_i} = \mathbf{v}_i^T \frac{(\hat{\mathbf{r}}_i \hat{\mathbf{r}}_i^T - I_3)}{\rho_i} \quad (19)$$

Where I_3 is the 3×3 identity matrix. It follows that the 1×2 Jacobian for the k th FDOA measurement is

$$-\lambda \frac{d\Delta f_k}{d\mathbf{x}} = \left[\frac{d\hat{\rho}_2}{d\mathbf{r}_2} - \frac{d\hat{\rho}_1}{d\mathbf{r}_1} \right] \Xi \quad (20)$$

where again Ξ is used to extract the first two elements of the range-rate difference Jacobian because they correspond to the partials with respect to \mathbf{x} .

One of the most common ways to solve the standard nonlinear least-squares problem is with the Gauss-Newton method, which starts with an initial guess for the state \mathbf{x}_0 , linearizes the measurement model function $\mathbf{h}(\mathbf{x})$ around the current best guess, and solves the linear least-squares problem. An increment to the current best estimate $\Delta\mathbf{x}$ is computed, and then the previous estimate is replaced by the new best estimate $\mathbf{x} + \Delta\mathbf{x}$ and iterates again.

Because this estimator is operating in the ENU frame, two additional steps must be taken. First, at the beginning of each iteration, the receivers' positions and velocities must be converted into the new ENU frame centered at the new

best estimate of the emitter position. This is accomplished by converting the current best emitter position estimate into the ECEF frame, so that the rotation matrix from ECEF to ENU can be determined. Secondly, when the new estimate of the state is computed ($\mathbf{x} + \Delta\mathbf{x}$), the increment $\Delta\mathbf{x}$ is in the current tangent East-North plane. When the new state is calculated, the estimated emitter position is no longer at the specified altitude constraint. To account for this, the new estimate must be converted to Latitude-Longitude-Altitude (LLA). The altitude corresponding to the new estimate must be replaced by the altitude constraint. A possible implementation of two-step geolocation starting from raw samples to final emitter position estimate is presented in algorithm 1.

Algorithm 1: TFDOA Geolocation

Input : Raw Samples, Altitude Constraint, Initial Guess

Output: Emitter Latitude and Longitude

```

1 Generate T/FDOA measurements
2 for  $t = 0: \text{end}$  do
3   | Generate CAF
4   | Get T/FDOA measurement
5 end
6 Nonlinear Estimation Gauss Newton
7 for  $i = 0: \text{end}$  do
8   | Convert receiver positions and velocities into the ENU frame
9   | Linearize about current estimate
10  | Solve NLLS, Compute state update
11  | Convert  $\hat{\mathbf{x}}$  to LLA and enforce altitude constraint
12 end
```

This two-step T/FDOA geolocation model can also be reduced to a TDOA-only solution or a FDOA-only solution. Those solutions can be used as a reasonableness test for the combined T/FDOA solution and to quantify the accuracy of the TDOA and FDOA measurements. The MLE of $\sigma_{\Delta\tau}^2$ and $\sigma_{\Delta f}^2$ can be calculated from the post-fit measurement residuals of the TDOA-only and FDOA-only solutions, respectively. Finally, if the user does not have a time history of the clock offset rate at each receiver, it can be modeled as a constant over short captures (e.g. less than 60 seconds [19]). The difference between the receiver clock offset rate can be added to the state as a bias term and can be estimated.

B. Direct Geolocation

The direct geolocation approach is a single-step grid-search method that solves directly for the emitter position without the need for intermediate T/FDOA measurements. The CAF is maximized directly by parameterizing the delay and Doppler time histories in terms of the emitter's position, as well as the known receivers' position, velocity, and clock time histories. It can be shown that for a large number of measurements the two-step approach is equivalent to the direct approach [27]. However, the direct approach outperforms the two-step approach in low SNR regimes and in cases limited to short captures. This estimator is proven to be maximum likelihood in [27].

A grid of three-dimensional emitter positions must be first designated. One approach is to create a rectangular grid in

latitude and longitude. Then, for each latitude and longitude pair, the altitude can be retrieved from a terrain model. This constrains the emitter position to the relative terrain on the surface of the Earth. Given that the emitter's position is assumed, and that the time history of receivers' position, velocity, and clock offset rate are known, the time history of TOAs and FOAs of a transmitted signal at each receiver can be computed with (3) and (8). It follows that a time history of TDOA and FDOA can be computed using (7) and (10).

Consider a time-synchronized capture between two receivers lasting T seconds producing N_s samples. Let f_s represent the sampling rate and T_s the time between samples. If the capture interval is short, it is appropriate to model both the time and frequency difference of arrival as constants. Let $\mathbf{t} = [t_0, t_1, \dots, t_{N_s-1}]$ denote the time vector containing the time of each sample with $t_0 = 0$, and t_k the time of the k th sample. For every candidate emitter position in the search space, the corresponding $\Delta\tau$ and Δf can be computed.

The digital representation of the signal $y_i(t)$ is given by $y_i[k] = y_i(kT_s)$. Let $\Delta\tilde{\tau} = \lfloor \Delta\tau \times f_s \rfloor$ denote the integer sample offset corresponding to $\Delta\tau$, where $\lfloor \cdot \rfloor$ denotes the round function. The position-domain correlation value is defined as

$$\tilde{S}(y_1[k], y_2[k], \Delta\tilde{\tau}, \Delta f) \triangleq \sum_{k=0}^{N_s-1} y_1[k] y_2^*[k + \Delta\tilde{\tau}] e^{-j2\pi\Delta f t_k} \quad (21)$$

The position corresponding to the $\Delta\tilde{\tau}$ and Δf values that maximize $|\tilde{S}(y_1[k], y_2[k], \Delta\tilde{\tau}, \Delta f)|$ is the maximum-likelihood emitter location.

Now consider a time-synchronized capture between two receivers for a longer interval. The TDOA and FDOA are not constant over longer integration intervals. If the TDOA and FDOA were erroneously assumed to be constant and (21) was used, the resulting grid of $|\tilde{S}|$ would appear as only noise. The signal would decorrelate because an incorrect frequency shift would have been applied. Thus, a more comprehensive model for the non-constant TDOA and FDOA time history is required.

Recall that a signal's instantaneous frequency is the time derivative of the phase $f(t) = d\theta(t)/dt$. Let $\Delta\Theta$ denote the $N_s \times 1$ vector containing a phase shift for each sample. For example, over a short capture as in (21), $\Delta\Theta = \Delta f \mathbf{t}$, which represents the time history of linearly increasing phase shifts. For a constant frequency shift, each sample gets a phase shift that increases linearly over time.

For intervals with a time-varying FDOA, a polynomial approximation of the FDOA time history is computed. This allows an instantaneous FDOA to exist at each sample and allows the time history of instantaneous frequency to be integrated to get instantaneous phase. This instantaneous phase can be used to get the corresponding vector of phase shifts $\Delta\Theta$ at each sample.

For a long capture interval producing N_s samples, a time history of TDOA $\Delta\tau$ and FDOA Δf measurements can be computed at each sample for every emitter position. A

polynomial approximation to $\Delta \mathbf{f}$ can be taken, and then integrated to get a phase shift time history $\Delta \Theta$.

Let $\Delta \tilde{\tau} = \lfloor \Delta \tau \times f_s \rfloor$ denote the integer sample offset vector corresponding to $\Delta \tau$. Let $\Delta \tilde{\tau}_k$ and $\Delta \Theta_k$ denote the k th element of $\Delta \tilde{\tau}$ and $\Delta \Theta$, respectively. The position-domain correlation value at a grid point is defined as

$$\tilde{S}(y_1[k], y_2[k], \Delta \tilde{\tau}, \Delta \Theta) \triangleq \sum_{k=0}^{N_s-1} y_1[k] y_2^*[k + \Delta \tilde{\tau}_k] e^{-j2\pi \Delta \Theta_k} \quad (22)$$

The position corresponding to the $\Delta \tilde{\tau}$ and $\Delta \mathbf{f}$ values that maximize $|\tilde{S}(y_1[k], y_2[k], \Delta \tilde{\tau}, \Delta \Theta)|$ is the maximum-likelihood emitter location. Fig. 2 shows an example of direct geolocation and an example implementation is presented in algorithm 2.

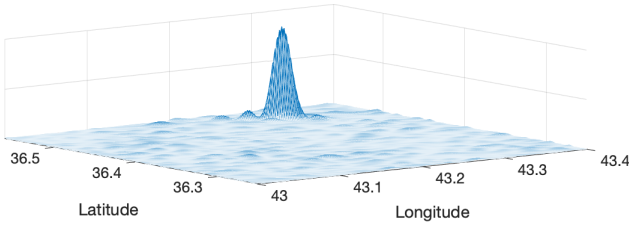


Fig. 2: Example position-domain correlation grid from direct geolocation for a single wideband emitter without any cyclostationary properties. The maximum value corresponds to the MLE of emitter’s position.

Algorithm 2: Direct Geolocation

Input : Raw Samples

Output: Emitter Position

- 1 Define the area of interest and determine a suitable grid of locations
 - 2 **for** *Position Grid* **do**
 - 3 Generate TDOA $\Delta \tau$ and FDOA $\Delta \mathbf{f}$ time history
 - 4 Obtain polynomial approximation to $\Delta \mathbf{f}$
 - 5 Integrate $\Delta \mathbf{f}$ to get $\Delta \Theta$
 - 6 Calculate $\tilde{S}(y_1[k], y_2[k], \Delta \tilde{\tau}, \Delta \Theta)$
 - 7 **end**
 - 8 The position corresponding to the maximum value of $|\tilde{S}(y_1[k], y_2[k], \Delta \tilde{\tau}, \Delta \Theta)|$ is the emitter position estimate.
-

One of the main advantages of the direct approach is that it enables longer coherent integration intervals of the received signals compared to the basic CAF in the two-step approach. For longer coherent integration times, the peak at the true emitter position becomes sharper and more pronounced. One drawback of longer integration intervals is that a finer grid is required. If the grid is too coarse, the peak will slip through the cracks leading to a missed detection.

Another advantage of direct positioning is that there will be a peak at every position where an emitter is located, provided that the emitter’s signal was strong enough to be received at both receivers. This is because, for a given position, only the signal at that position will correlate. The other signals in

the capture will become decorrelated and appear as noise. The height of the peak is dependent on the emitter’s transmit power, as the louder a signal is, the more pronounced the peak will be. Finally, this technique works for any waveform—including those exhibiting cyclostationarity. Noncoherently combining position-domain correlations prunes any structures due to repetition in the transmitted waveform as well as any spurious peaks due to noise.

IV. A RECENT REAL-WORLD CAPTURE

This section describes the dual-receiver platform and spectral characteristics of two capture events during April 2022 over the Eastern Mediterranean.

A. Spire Satellites

Spire Global Inc. operates a global network of over 120 satellites. Among these satellites, are about 60 *STRATOS* satellites, whose original purpose was GNSS radio occultation (GNSS-RO), that can be repurposed for geolocation of emitters operating in the GPS L1 and L2 bands. The *STRATOS* satellites carry one wide-field-of-view zenith-facing antenna for precise orbit determination, and one or two Earth-limb-facing narrow-field-of-view high-gain antennas. *STRATOS*’s RF circuitry has three dual-frequency channels, with each antenna connected to one of the front end channels. Digitization of each signal happens coherently based on a single sampling clock. Simultaneous collections of the 2-bit quantized 6.2 Msps raw intermediate frequency (IF) samples centered at GPS L1 and L2 can be performed. These data can be packaged and downlinked through Spire’s network of dedicated ground stations.



Fig. 4: Ground tracks of a pair of LEO-based receivers during the two 60-second captures over the Eastern Mediterranean. Both satellites are moving from north to south.

During April 2022, two *STRATOS* satellites performed two consecutive 60-second simultaneous capture events separated by 180 seconds, while over the Eastern Mediterranean as shown in Fig. 4. During each 60-second capture, the satellites had an average altitude of 524 km and an average velocity of 7,678 m/s, traveling from north to south. The forward-facing antenna was used for the raw capture in the first simultaneous event, and the backward facing antenna was used during the

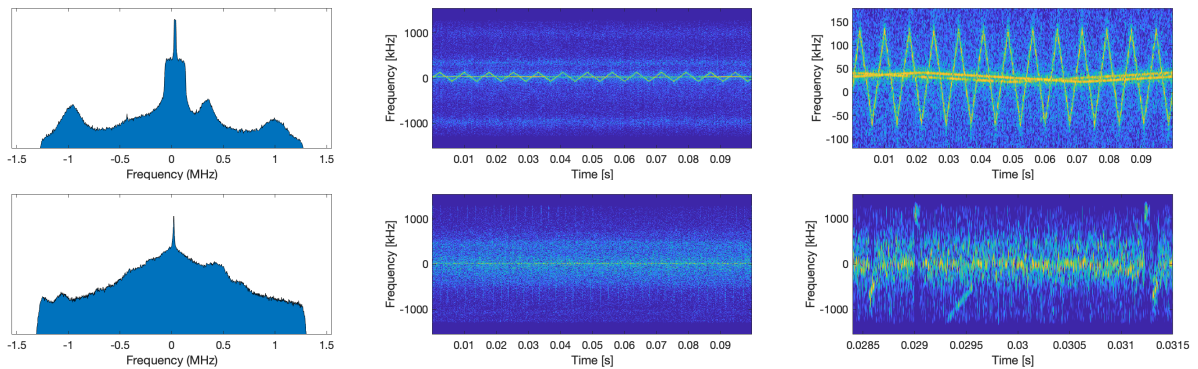


Fig. 3: Power spectra (left), spectrogram (middle), and zoomed in spectrogram (right) centered at the GPS L1 (top row) and L2 (bottom row) frequencies from interference-affected data captured in April 2022. By visual inspection on the spectrograms on the right, L1 contains multiple CW chirp jammers, as well as other wideband interference. L2 contains both narrowband and wideband interference. Furthermore, this capture included multiple long range air surveillance radars operating near GPS L2.

second simultaneous event. The precise orbit determination antenna on each satellite was used to calculate the onboard navigation solution, which includes receiver position, velocity, clock bias, and clock offset rate estimates. The raw samples from the GNSS-RO antennas and the onboard navigation solution were downlinked for post-processing.

B. Spectrum Analysis

Fig. 3 illustrates the captured signals’ spectral characteristics during the first simultaneous capture event. There is composite wideband interference on both GPS L1 and L2. GPS L1 and L2 matched-code jammers were present. However, they could not be tracked due to the harsh jamming environment. Visual inspection of the spectrogram indicate that L1 contains multiple CW chirp jammers as well as other wideband interference. The wider-bandwidth chirp jammer had a bandwidth of approximately 200 kHz and a period of 8 ms. The narrower-bandwidth chirp jammers had a bandwidth of approximately 20 kHz and a period of 100 ms. The 20 kHz chirp jammers have the same parameters of a jammer previously captured in the Eastern Mediterranean [10].

L2 contains a particularly strong narrowband jammer as well as other wideband interference. Throughout the captures, multiple long range air surveillance radars operating near GPS L2 are visible. Various types of long-range radar systems operate in the L-band [35]. Every so often, the receivers captured a strong three-dimensional search radar that saturated the automatic gain control onboard the satellites.

V. EMITTER GEOLOCATION

This section discusses two-step and direct geolocation of the emitters captured in the Spire dataset. The results focus on the geolocation of a known GNSS jammer operating out of Khmeimim Air Base on the coast of Syria. Additionally, the advantages of direct geolocation are showcased for low SNR signals, short time captures, crowded signal environments, and for signals exhibiting cyclostationarity. Wide-area GNSS in-

terference monitoring via direct geolocation reveals numerous jammers across Syria, Turkey, Iraq, Ukraine, and Israel.

A. Two-Step Geolocation

The CAF on L2 from the first simultaneous capture is shown in Fig. 6. The L2 CAF is what one would expect to find when computing a CAF: sharp peaks among noise.

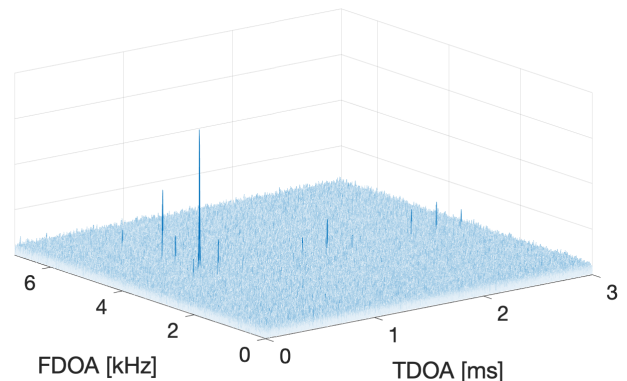


Fig. 6: CAF for L2 during the first simultaneous capture. There are multiple spatially-separated emitters present in this CAF. There are three signals exhibiting cyclostationary around 3 kHz, repeating every millisecond.

In the L2 CAF, there are multiple spatially-separated emitters present, deduced from the multiple peaks. Because the emitters are spatially diverse, the relative geometries between each emitter and the LEO-based receivers evolve differently over the duration of the capture. The more spatially diverse the emitters are, the more separated the peaks in the CAF become. Had the emitters been close to each other, they would have similar T/FDOA measurements, leading to closely-spaced peaks in the CAF, making tracking the multiple peaks difficult. The magnitude of the peaks can determine the relative power of each emitter, so long as the antennas on the receivers had an identical antenna gain at each emitter. Additionally,

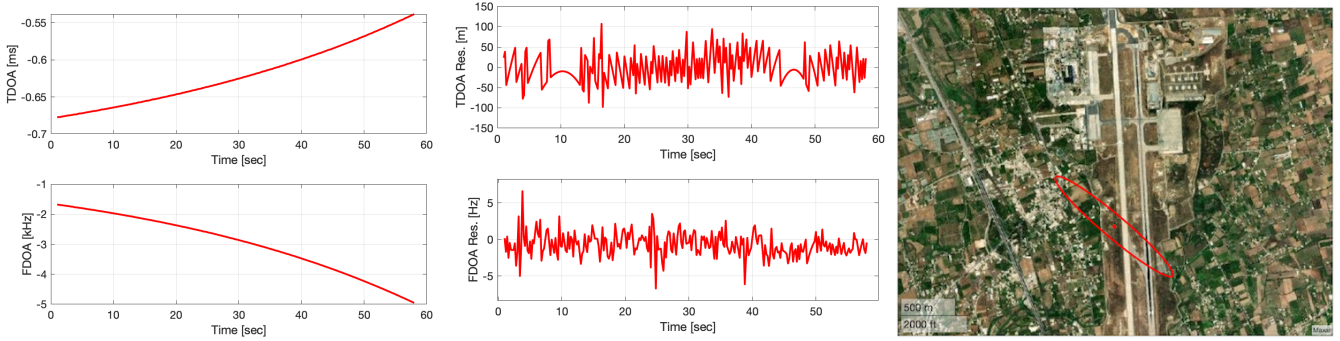


Fig. 5: **Left:** The time history of TDOA and FDOA measurements corresponding to the largest peak in the L2 CAF. **Middle:** The TDOA and FDOA residuals from the nonlinear least squares estimator. **Right:** The final two-step T/FDOA geolocation estimate converges to Khmeimim Air Base on the coast of Syria, which has been previously discovered to have transmitted GPS jamming signals [19]. The semi-major and semi-minor axes of the 95% ellipse are 619 and 77 meters, respectively.

cyclostationary signals manifest repeating patterns in the CAF, as shown by the run of peaks around 3 KHz in Fig. 6.

Fig. 5 shows the time history of TDOA and FDOA measurements corresponding to the largest peak in the L2 CAF over the 60-second capture. These measurements were taken at 5 Hz and then served to the nonlinear estimator. The final two-step emitter position estimate is displayed in Fig. 5. The final solution converged to Khmeimim Air Base on the coast of Syria, which has been previously discovered to host a powerful GPS jammer [19].

The TDOA and FDOA residuals from the nonlinear least-squares estimator are also shown in Fig. 5. They are zero-mean and Gaussian distributed, indicating that the presented measurement model is accurate. The TDOA residuals time history appears to have unexpected structure; this structure arises due to the range resolution from the sampling rate. The TDOA measurement resolution is limited by the sampling rate. Because the sampling rate at baseband is 3.1 Msps, the range resolution is 96.7 m. As a consequence, the TDOA residuals appear to have structure. The TDOA residuals remain between the range resolution of ± 96.7 m, meaning the expected performance with the sampling rate was achieved.

The cost surface for the calculated set of T/FDOA measurements corresponding to the jammer at the Khmeimim Air Base is shown in Fig. 7. The top plot is the TDOA-only cost surface, the middle plot is the FDOA-only cost surface, and the bottom plot is the T/FDOA cost surface. The global minimum of each cost surface aligns with Khmeimim Air Base.

The capture's specific receiver geometry gives rise to a reflection point on the opposite side of the satellites' average ground track. For a single T/FDOA measurement pair, the true emitter position and the alias are indistinguishable. The ambiguity between these points begins to resolve if the baseline between the receivers changes with each T/FDOA measurement pair. Each T/FDOA measurement pair in the time series will have a different alias location because of the time-varying baseline between the receivers. Conversely, each T/FDOA measurement pair in the time series will be consistent with the true emitter position, resolving the ambiguity.

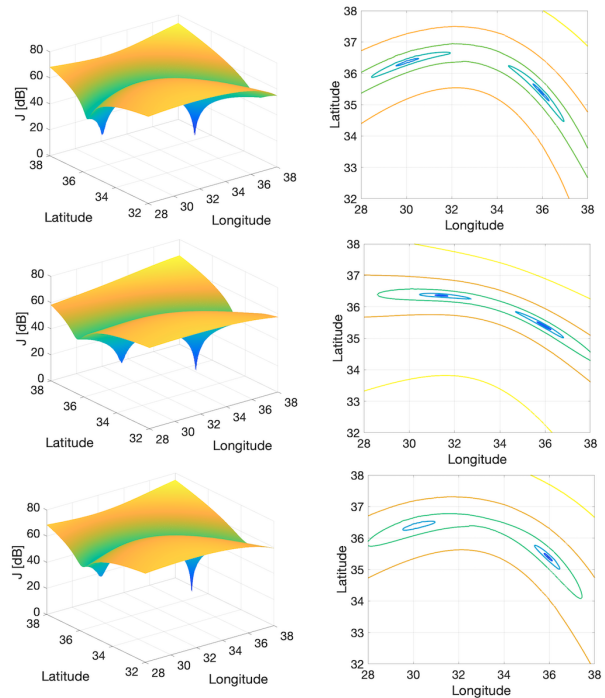


Fig. 7: Cost surface for TDOA (top), FDOA (middle), and T/FDOA (bottom) with the set of measurements corresponding to the Khmeimim Air Base jammer.

Table I provides an example of how capture duration and receiver geometry affect the formal error ellipse of the two-step geolocation estimate for the jammer at the Khmeimim Air Base in Syria during the first simultaneous capture event. As the duration of the capture increases, the error ellipse reduces significantly. Furthermore, there is a stark difference between using the first five seconds at the beginning of the capture, versus the final five seconds at the end of the capture. This is due to receiver geometry: there is more change in the geometry between the receivers and the emitter during the final five seconds. There is more information in the measurements when there is greater change in geometry.

Duration (sec)	Start		End	
	95% semi-major (m)	95% semi-minor (m)	95% semi-major (m)	95% semi-minor (m)
5	4737	570	1953	238
10	3193	387	1431	176
20	2022	252	1072	135
30	1454	188	913	119
60	619	77	619	77

TABLE I: The 95% formal error ellipse in meters from two-step geolocation for the jammer at Khmeimim Air Base in Syria during the first simultaneous event. The left pair of 95% semi-major and semi-minor axes were from measurements from beginning of the capture, and the right pair were from the end. This table demonstrates how geometry and the duration of capture affects the two-step geolocation solution.

B. Effects of Signal Cyclostationarity

Cyclostationary signals, such as chirp jammers, give rise to structures in the CAF that make it harder to track individual emitters. Identification and tracking becomes especially challenging when there are multiple cyclostationary emitters with overlapping frequency content and a wide range of received power, in which case the T/FDOA measurement domain becomes highly structured with features ambiguously related to the emitters involved. The L1 CAF is shown in Fig. 8. Recall that the strongest signals on L1 are the chirp jammers. Because the chirp jammers are so powerful, it is difficult to detect any other signals in the CAF. An autonomous multi-peak tracking algorithm would struggle in scenarios with multiple emitters having cyclostationary signals.

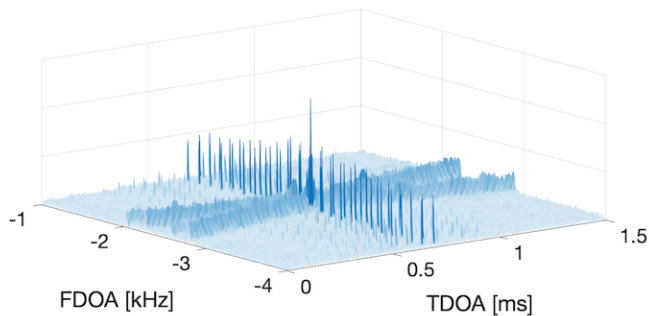


Fig. 8: L1 CAF during the first simultaneous capture. The chirp jammers are so powerful that no other emitters appear in the CAF.

From the top-down view in Fig. 9 one can see that each chirp jammer creates an “X” shape in the CAF, where the center is the true TDOA and FDOA of the signal. The higher-bandwidth chirp jammer can be isolated from the lower-bandwidth chirp jammers by simply using a high pass filter. An identical X repeats in the CAF every eight milliseconds due to cyclostationarity. A cyclostationary signal will create N number of repeating peaks in the CAF, where N is the number of cycles a signal repeats within the CAF time duration. This behavior was also observed with the cyclostationary signals in the L2 CAF.

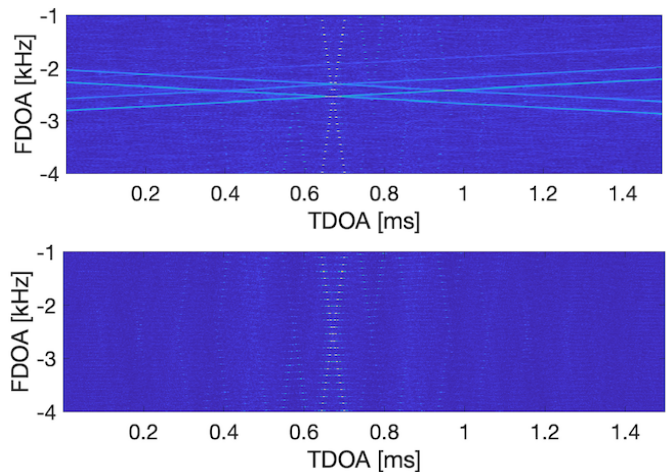


Fig. 9: Top-down view of the L1 CAF. Diamond structures created by the strong periodic chirps are formed. The higher-bandwidth jammer can be isolated with a high pass filter.

In the case of the two identical lower-bandwidth chirp jamming signals, their X’s overlap, creating a diamond formation with a peak at each vertex. The ambiguous diamond shape in the CAF is an artifact of the signal structure and cannot be removed by filtering. One way to deal with the four peaks from two signals is to track all four peaks. If the emitter is assumed to be stationary and constrained to the surface of the Earth, it will be likely that only two of the peaks correspond to reasonable geolocation solutions. Additionally, the geometry of the receivers can be used to determine which are false peaks. The TDOA and FDOA measurements can be bounded due to the receivers’ geometry.

C. Direct Geolocation

Fig. 10 shows the position-domain correlation values over the Khmeimim Air Base using the L2 raw samples with various integration times. Each point in the grid was separated by $.0005^\circ$ in latitude and longitude. For each latitude and longitude pair, the surface altitude was retrieved from a terrain model. The global elevation model used was the Global Multi-resolution Terrain Elevation Data 2010 (GMTED2010) developed by the U.S. Geological Survey and the National Geospatial-Intelligence Agency. The elevation is measured relative to mean sea level using Earth gravitational model EGM-96. The root mean square error is approximately 26 meters.

The maximum peak in the position-domain correlation function for the various integration intervals in Fig. 10 is nearly equivalent to the two-step solution. This is expected because in the high SNR scenarios with long captures, the two-step and one-step solutions are equivalent. In the one-step approach, the effects of integration interval length are apparent in Fig. 10. As the integration time increases, the peak becomes sharper and more pronounced. This is because over longer intervals, the signal decorrelates more quickly for incorrect emitter positions. The more wideband the signal is, the more quickly it decorrelates and the peak becomes sharper.

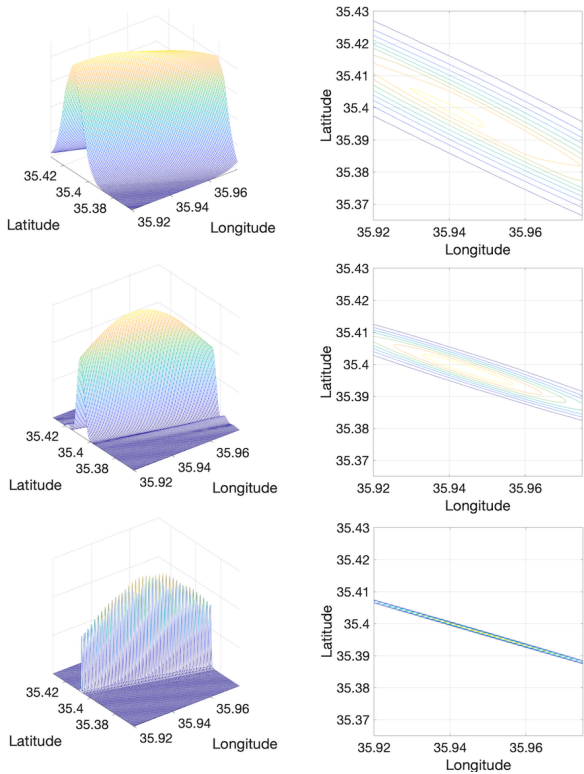


Fig. 10: Direct geolocation position-domain correlation grid over Khmeimim Air Base for (top) 20-ms, (middle) 100-ms, and (bottom) 1-second integration times.

A consequence of longer coherent integration is that a finer grid spacing is required. If wide-area surveillance is desired, one might opt for a coarse grid covering a large area paired with shorter integration intervals. After getting a general sense of the emitters' locations via the course grid, a finer grid with longer integration intervals can be used to get more accurate geolocation estimates.

Fig. 11 demonstrates how direct geolocation is better suited for processing captures with structured, cyclostationary signals. The position-domain correlation function for the chirp jammer is shown at the beginning (top graph) and end (middle graph). There is structure in both, but that structure changes with the instantaneous receivers' geometry, which changes over time. When multiple position-domain accumulations are noncoherently combined, all of the false peaks are reduced below the noise floor, while the main peak corresponding to the true emitter position remains. The position of the higher-bandwidth chirp jammer is estimated to be in northern Israel. Noncoherent integration is a powerful tool that can suppress spurious false peaks from waveform structure and cyclostationarity.

Fig. 12 shows direct geolocation over Syria with the L2 data. A 100 ms accumulation was taken once per second, over 58 seconds. The 58 position-domain correlations were noncoherently combined. Each peak corresponds to an emitter position estimate, with the largest peak corresponding to Khmeimim Air Base. The receivers' geometry also heavily

affects correlation in the position domain. There was better receiver geometry for the transmitters on the east-side, resulting in sharper peaks.

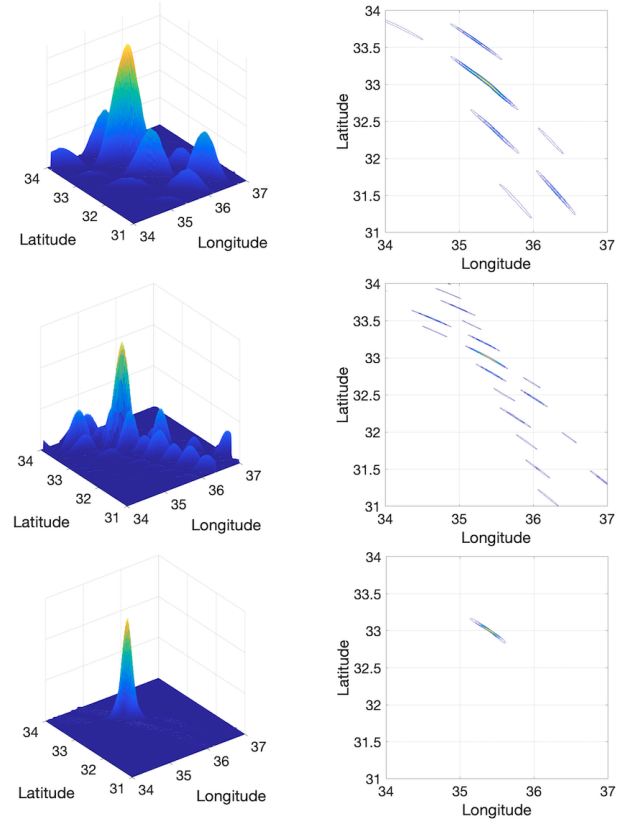


Fig. 11: Direct geolocation on the chirp jammer in the beginning (top) and end (middle) of the capture. A 100 ms accumulation was taken once every 5 seconds. The eleven position-domain correlations were noncoherently combined, shown at the bottom. Noncoherent integration is a powerful tool that suppresses the spurious false peaks from waveform structure and cyclostationarity.

This position-domain correlation was repeated for L1 on the first capture and L1 and L2 on the second capture. The peaks from the position domain correlations on both captures and frequencies are shown in Fig. 13. Each one of these estimates is plausible, given the agreement between both frequencies and passes, as well as the surrounding equipment near each estimate. This also showcases the superiority of the direct approach in crowded signal environments. The two-step approach would have depended on an additional complex multi-peak tracking and association algorithm to generate a time series of T/FDOA measurements, whereas in the direct approach the emitter position estimate comes directly from the raw samples.

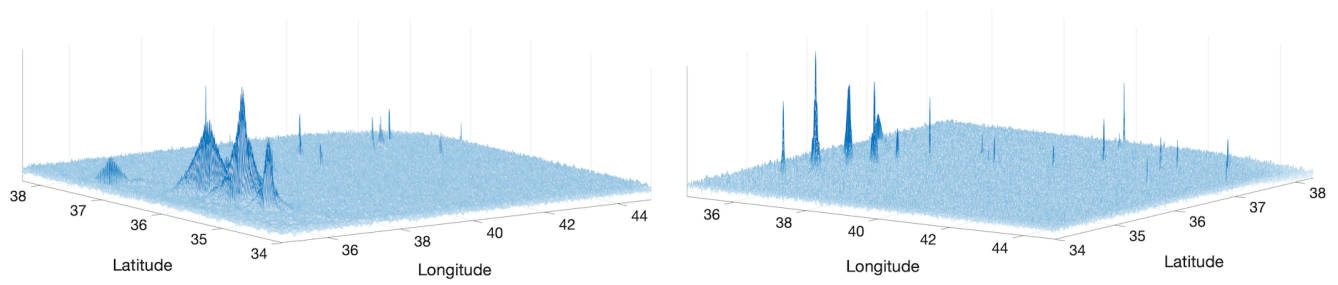


Fig. 12: Direct geolocation over Syria with two different views of the position domain. A 100-ms accumulation was taken once per second, over 58 seconds. Shown here are 58 position-domain correlations noncoherently combined. Each peak corresponds to an emitter position estimate.

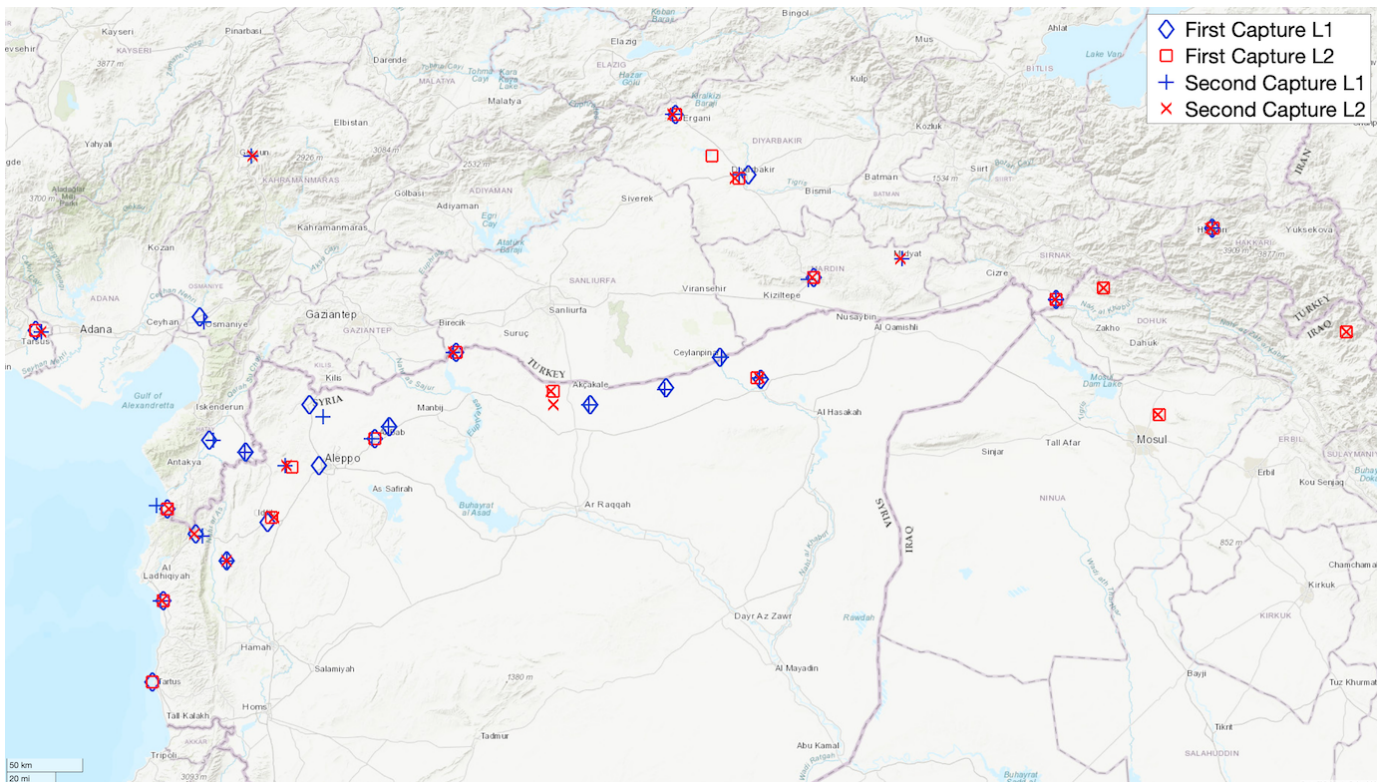


Fig. 13: Final emitter position estimates on L1 and L2 across both simultaneous captures from direct geolocation. All emitters were assumed to be stationary and constrained to the surface of the Earth.

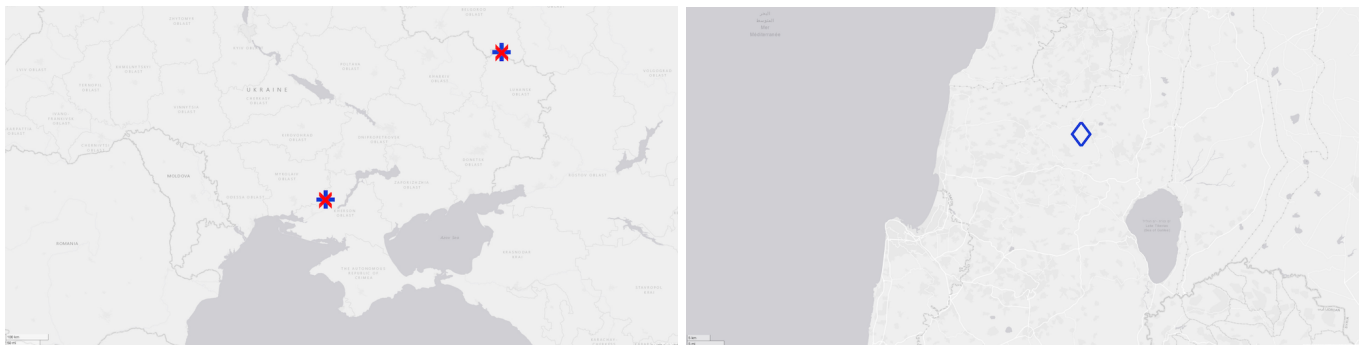


Fig. 14: Jammers found in Ukraine (left) and Israel (right).

VI. CONCLUSION

This paper explored two-step and direct geolocation of terrestrial emitters from LEO. The full algorithms for two-step and single-step direct geolocation were presented. It was demonstrated that the direct approach is a powerful geolocation technique for low SNR signals during short captures with multiple emitters. This paper also investigated emitter geolocation in crowded signal environments and explored geolocating cyclostationary signals. The effects of interference signal time correlation on the two-step approach's complex ambiguity function were investigated. Finally, this paper demonstrated two-step and direct geolocation on raw intermediate frequency samples recorded from Spire Global's LEO constellation. Recent real-world GNSS interference signals captured by two time-synchronized LEO receivers over the Eastern Mediterranean were characterized and their emitters geolocated.

ACKNOWLEDGMENTS

Research was sponsored by the U.S. Department of Transportation (USDOT) under the University Transportation Center (UTC) Program Grant 69A3552047138 (CARMEN), and by affiliates of the 6G@UT center within the Wireless Networking and Communications Group at The University of Texas at Austin.

REFERENCES

- [1] T. E. Humphreys, "Statement on the vulnerability of civil unmanned aerial vehicles and other systems to civil GPS spoofing," *United States House of Representatives Committee on Homeland Security: Subcommittee on Oversight, Investigations, and Management*, July 2012.
- [2] M. L. Psiaki and T. E. Humphreys, "GNSS spoofing and detection," *Proceedings of the IEEE*, vol. 104, no. 6, pp. 1258–1270, 2016.
- [3] Z. Clements, J. E. Yoder, and T. E. Humphreys, "Carrier-phase and IMU based GNSS spoofing detection for ground vehicles," in *Proceedings of the ION International Technical Meeting*, Long Beach, CA, 2022, pp. 83–95.
- [4] T. E. Humphreys, "Interference," in *Springer Handbook of Global Navigation Satellite Systems*. Springer International Publishing, 2017, pp. 469–503.
- [5] D. Borio, C. O'Driscoll, and J. Fortuny, "GNSS jammers: Effects and countermeasures," in *2012 6th ESA Workshop on Satellite Navigation Technologies (Navitec 2012) & European Workshop on GNSS Signals and Signal Processing*. IEEE, 2012, pp. 1–7.
- [6] Z. Clements, J. E. Yoder, and T. E. Humphreys, "GNSS spoofing detection," *GPS World*, vol. 34, no. 2, pp. 36–41, 2023.
- [7] Z. Liu, S. Lo, T. Walter, and J. Blanch, "Real-time detection and localization of GNSS interference source," in *Proceedings of the 35th International Technical Meeting of the Satellite Division of The Institute of Navigation (ION GNSS+ 2022)*, 2022, pp. 3731–3742.
- [8] M. Dacus, Z. Liu, S. Lo, and T. Walter, "Improved RFI localization through aircraft position estimation during losses in ADS-B reception," in *Proceedings of the 35th International Technical Meeting of the Satellite Division of The Institute of Navigation (ION GNSS+ 2022)*, 2022, pp. 947–957.
- [9] O. Osechas, F. Fohlmeister, T. Dautermann, and M. Felix, "Impact of GNSS-band radio interference on operational avionics," *NAVIGATION: Journal of the Institute of Navigation*, vol. 69, no. 2, 2022.
- [10] E. P. Marcos, A. Konovaltsev, S. Caizzone, M. Cuntz, K. Yinusa, W. Elmarissi, and M. Meurer, "Interference and spoofing detection for GNSS maritime applications using direction of arrival and conformal antenna array," in *Proceedings of the 31st International Technical Meeting of The Satellite Division of the Institute of Navigation (ION GNSS+ 2018)*, 2018, pp. 2907–2922.
- [11] R. Mitch, R. Dougherty, M. Psiaki, S. Powell, B. O'Hanlon, J. Bhatti, and T. Humphreys, "Signal characteristics of civil GPS jammers," in *Proceedings of the ION GNSS Meeting*, 2011.
- [12] R. Mitch, M. Psiaki, and T. Ertan, "Chirp-style GNSS jamming signal tracking and geolocation," *NAVIGATION: Journal of the Institute of Navigation*, vol. 63, no. 1, pp. 15–37, 2016.
- [13] J. A. Bhatti, T. E. Humphreys, and B. M. Ledvina, "Development and demonstration of a TDOA-based GNSS interference signal localization system," in *Proceedings of the IEEE/ION PLANS Meeting*, April 2012, pp. 1209–1220.
- [14] D. Musicki, R. Kaune, and W. Koch, "Mobile emitter geolocation and tracking using TDOA and FDOA measurements," *Signal Processing, IEEE Transactions on*, vol. 58, no. 3, pp. 1863–1874, March 2010.
- [15] H. Witzgall, "Two-sensor tracking of maneuvering transmitters," in *2018 IEEE Aerospace Conference*. IEEE, 2018, pp. 1–7.
- [16] N. Okello, "Emitter geolocation with multiple UAVs," in *2006 9th International Conference on Information Fusion*. IEEE, 2006, pp. 1–8.
- [17] R. J. Bamberger, J. G. Moore, R. P. Goonasekeram, and D. H. Scheidt, "Autonomous geolocation of RF emitters using small, unmanned platforms," *Johns Hopkins APL technical digest*, vol. 32, no. 3, pp. 636–646, 2013.
- [18] D. M. LaChapelle, L. Narula, and T. E. Humphreys, "Orbital war driving: Assessing transient GPS interference from LEO," in *Proceedings of the ION GNSS+ Meeting*, St. Louis, MO, 2021.
- [19] M. J. Murrian, L. Narula, P. A. Iannucci, S. Budzien, B. W. O'Hanlon, S. P. Powell, and T. E. Humphreys, "First results from three years of GNSS interference monitoring from low Earth orbit," *Navigation, Journal of the Institute of Navigation*, vol. 68, no. 4, pp. 673–685, 2021.
- [20] Z. Clements, P. Ellis, M. L. Psiaki, and T. E. Humphreys, "Geolocation of terrestrial GNSS spoofing signals from low Earth orbit," in *Proceedings of the ION GNSS+ Meeting*, Denver, CO, 2022, pp. 3418–3431.
- [21] P. Ellis, D. V. Rheeden, and F. Dowla, "Use of Doppler and Doppler rate for RF geolocation using a single LEO satellite," *IEEE Access*, vol. 8, pp. 12 907–12 920, 2020.
- [22] P. B. Ellis and F. Dowla, "Single satellite emitter geolocation in the presence of oscillator and ephemeris errors," in *2020 IEEE Aerospace Conference*. IEEE, 2020, pp. 1–7.
- [23] P. Ellis and F. Dowla, "Performance bounds of a single LEO satellite providing geolocation of an RF emitter," in *2018 9th Advanced Satellite Multimedia Systems Conference and the 15th Signal Processing for Space Communications Workshop (ASMS/SPSC)*. IEEE, 2018, pp. 1–5.
- [24] A. Sidi and A. Weiss, "Delay and Doppler induced direct tracking by particle filter," *Aerospace and Electronic Systems, IEEE Transactions on*, vol. 50, no. 1, pp. 559–572, January 2014.
- [25] K. Ho and Y. Chan, "Geolocation of a known altitude object from TDOA and FDOA measurements," *IEEE Transactions on Aerospace and Electronic Systems*, vol. 33, no. 3, pp. 770–783, July 1997.
- [26] D. Haworth, N. Smith, R. Bardelli, and T. Clement, "Interference localization for EUTELSAT satellites—the first European transmitter location system," *International journal of satellite communications*, vol. 15, no. 4, pp. 155–183, 1997.
- [27] A. Weiss, "Direct geolocation of wideband emitters based on delay and Doppler," *Signal Processing, IEEE Transactions on*, vol. 59, no. 6, pp. 2513–2521, June 2011.
- [28] J. Bhatti, "Sensor deception detection and radio-frequency emitter localization," Ph.D. dissertation, The University of Texas at Austin, Aug. 2015.
- [29] A. M. Reuven and A. J. Weiss, "Direct position determination of cyclostationary signals," *Signal Processing*, vol. 89, no. 12, pp. 2448–2464, 2009.
- [30] J. Li, L. Yang, F. Guo, and W. Jiang, "Coherent summation of multiple short-time signals for direct positioning of a wideband source based on delay and Doppler," *Digital Signal Processing*, vol. 48, pp. 58–70, 2016.
- [31] T. Tirer and A. J. Weiss, "High resolution localization of narrowband radio emitters based on Doppler frequency shifts," *Signal Processing*, vol. 141, pp. 288–298, 2017.
- [32] A. Rihaczek, *Principles of high-resolution radar*. McGraw-Hill, 1969.
- [33] S. Stein, "Differential delay/Doppler ML estimation with unknown signals," *Signal Processing, IEEE Transactions on*, vol. 41, no. 8, pp. 2717–2719, Aug. 1993.
- [34] S. Mohiuddin and M. Psiaki, "Carrier-phase differential Global Positioning System navigation filter for high-altitude spacecraft," *Journal of Guidance, Control, and Dynamics*, vol. 31, no. 4, pp. 801–814, 2008.
- [35] "1215-1240 MHz." [Online]. Available: https://www.ntia.doc.gov/files/ntia/publications/compendium/1215.00-1240.00_01MAY15.pdf